arXiv:1609.09204v1 [cond-mat.mes-hall] 29 Sep 2016

Design a giant-gap 3D topological insulator: The case of double perovskites

Shu-Ting Pi,* Hui Wang,* Jeongwoo Kim, and Ruqian Wu†

Department of Physics and Astronomy,

University of California, Irvine, California 92697-4575, USA

Yin-Kuo Wang‡

Center of General Education, National Taiwan Normal University, Taipei 116, Taiwan

Chi-Ken Lu§

Department of Physics, National Taiwan Normal University, Taipei 11677, Taiwan

Abstract

We propose a new approach to find three-dimensional topological insulators (TIs) in which the spin-orbit coupling (SOC) can more effectively generate a band gap. The band gap of conventional TI such as Bi_2Se_3 is mainly limited by two factors, the strength of SOC and, from electronic structure perspective, the band gap when SOC is absent. While the former is an atomic property, we find that the latter can be minimized in a generic rock-salt lattice model in which band touching *at* the Fermi level along with band inversion takes place in the absence of SOC. Thus, giant-gap TI's or TI's comprised of lighter elements are expected. The model applies to a class of double perovskites A_2BiXO_6 (A = Ca, Sr, Ba; X = Br, I) and the band gap is predicted up to 0.55 eV, much larger than known *pristine* 3D TIs. Besides, the doped compounds might turn into topological superconductors at low temperature since the Bloch states near the Fermi level are unaltered by the dopant at A-site. First-principle calculations considering realistic surface indicate that the Dirac cones are stabilized if proper termination is chosen. The mechanism is general and may open a new vista for future TI-based electronic devices.

Introduction. The discovery of topological phases of matter such as quantum Hall effect [1, 2], quantum spin Hall effect [3–5], topolocial crystalline insulators [6], Dirac semimetals [7, 8] and Weyl semimetals [9, 10] along with the classifications [11–13] is a remarkable success of condensed matter physics and material science. The exotic phenomena rooted in the Dirac electrons on the surface of topological insulators (TIs) [14–19] have spurred a bulk of interdisciplinary effort in searching new science and functional materials for practical appliactions [20–22].

TIs with large band gaps are particularly desired in achieving room-temperature applications. Tetradymite materials such as Bi_2Se_3 [23] and other combinations of heavy elements from the V and VI families (see Table I in Ref. [19]) are the prototypical 3D TIs which have demonstrated characteristic behaviors of the surface Dirac fermions [16, 17] but at fairly low temperature due to small bulk band gap. Unlike semiconductors, the band gap of TI results from intrinsic spin-orbit coupling (SOC). For 2D materials, the band gap can be increased in a variety of ways, from incorporating heavy adatoms [24], halogenation [25], to choosing appropriate substrates [26] because of the open structure. As for 3D materials, on the other hand, there is little room for tuning the electronic structure and band gap; selecting heavier constituents and/or changing lattice structures seem to be the only feasible route.

Fig.1(a) shows the typical evolution of electronic structure during a hypothetical process of turning on the SOC to its full strength. The topological phase transition goes through the three stages: shrinking of band gap (I), gap closing (II), and reemergence of a gap in the topological phase (III and IV) [27]. Therefore, from band structure perspective, the gap in the absence of SOC (stage I) seems to undermine the effectiveness of SOC in generating a giant band gap in the topological phase. Here, we propose that the transition in Fig. 1(b) may suggest a different way to make SOC more *effective*. Namely, materials possessing band touching at the Fermi level [28–30] in the absence of SOC may become giant-gap TIs once the SOC sets in.

In this work, a tight-binding (TB) model of rock-salt lattice with the unit cell containing a pair of s and p orbitals from two atoms is proposed to implement the novel topological phase transition depicted in Fig.1(b). With such TB model, one may start with a band insulator in which the valence band is of s character and the conduction band is degenerate and of p character. By tuning a set of TB parameters, we are able to achieve the band structure in which the valence and conduction bands, now both having p character, touch *at*

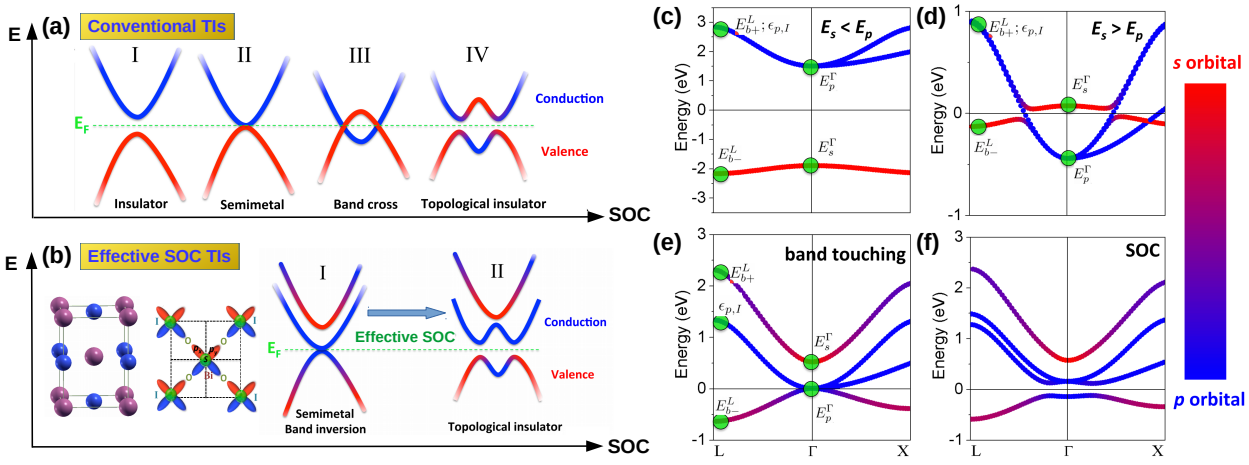

FIG. 1. (color online) Topological phase transitions that lead to (a) conventional TIs and (b) our proposed TIs due to an *effective* SOC. Inset in (b) shows the rock salk structure and its orbitals of our proposed tight-binding model in Eq. 1. (c)-(f) display the bulk spectra by varying the parameters in text. (c) Topological trivial state with the s-character Bloch state just below Fermi level at Γ point. (d) Band inversion with the s-character state above the p-character one. (e) Band touching occurs when $E_s^\Gamma > E_p^\Gamma > E_{b-}^L$ is satisfied. (f) Finally the SOC is turned on and a gap is opened. The Bloch state just below the Fermi level now has the p-character and the topologically nontrivial state is arrived.

the Fermi energy, which is protected by the cubic symmetry, and the band of s character lies above them. Consequently, even with a weak SOC, the band touching at the Fermi energy is lifted at once and the highest Bloch state of valence band is of p character. This flip of band character indicates the change of topological nature of the material.

More importantly, the band touching at the Fermi level and the accompanying band inversion are shown to be universal among the materials reported in this paper. Based on the first-principle calculation and Z_2 index evaluation, the double perovskites A_2BiXO_6 (A = Ca, Sr, Ba; X = I, Br) are TI's and the largest band gap is 0.55 eV, much larger than known *pristine* 3D TIs. Further confirmation by employing the Wannier function-based tight-binding calculation allows us to see the Dirac spectrum of the surface states. Since perovskites are stable materials with variable properties by doping, the reported materials could add to the already diverse functionality of perovskites which has been intensively studied. [31–36]

Tight-binding model. Band touching in the known materials, graphene for instance, often

implies some discrete symmetry from the lattice [12]. Here, we introduce a generic tight-binding model for rock-salt lattice from which a band touching at Γ point emerges if the band energies at L and Γ around the Fermi level are properly ordered. Here, we consider the rock-salt lattice occupied by Bi and I atoms with each contributing one s-orbital and three p-orbitals. Dictated by the cubic symmetry, the tight-binding Hamiltonian in momentum space reads

$$H_{TB} = \begin{pmatrix} H_s & T_x & T_y & T_z \\ T_x^\dagger & H_{p_x} & 0 & 0 \\ T_y^\dagger & 0 & H_{p_y} & 0 \\ T_z^\dagger & 0 & 0 & H_{p_z} \end{pmatrix} \tag{1}$$

in the representation of the eight atomic orbitals, $[\mathrm{I}_s, \mathrm{Bi}_s, \mathrm{I}_{p_x}, \mathrm{Bi}_{p_x}, \mathrm{I}_{p_y}, \mathrm{Bi}_{p_y}, \mathrm{I}_{p_z}, \mathrm{Bi}_{p_z}]^T$. The spin is suppressed for the moment, and each element in the matrix is in fact a two-by-two matrix. The diagonal ones read

$$H_s = \begin{pmatrix} \epsilon_{s,\mathrm{I}} & 2t_{ss}\sum_i \cos\frac{k_i a_i}{2} \\ 2t_{ss}\sum_i \cos\frac{k_i a_i}{2} & \epsilon_{s,\mathrm{Bi}} \end{pmatrix}, \tag{2}$$

and

$$H_{p_x} = \begin{pmatrix} \epsilon_{p,\mathrm{I}} & 2\sum_i t_{pp}^{\sigma/\pi} \cos\frac{k_i a_i}{2} \\ 2\sum_i t_{pp}^{\sigma/\pi} \cos\frac{k_i a_i}{2} & \epsilon_{p,\mathrm{Bi}} \end{pmatrix}, \tag{3}$$

which are responsible for the coupling between orbitals from different atoms but of the same symmetry. For shorter notation, the sum in the off-diagonal element of H_{p_x} reads $t_{pp}^{\sigma}\cos\frac{k_x a_x}{2} + t_{pp}^{\pi}(\cos\frac{k_y a_y}{2} + \cos\frac{k_z a_z}{2})$. Similar expressions in H_{p_y} and H_{p_z} can be inferred from the cubic symmetry. The s and p-orbitals are coupled by the off-diagonal matrices, $T_i = (2i)t_{sp}\sin\frac{k_i a_i}{2}\sigma_x$, with $i = x, y, z$, and σ_x being the first of three Pauli matrices. In the followings, we assume the order of orbital energies: $\epsilon_{s,\mathrm{I}} < \epsilon_{s,\mathrm{Bi}} < \epsilon_{p,\mathrm{I}} < \epsilon_{p,\mathrm{Bi}}$. Besides, the Fermi level is above the second lowest band and below the third lowest band of the matrix in Eq. 1.

At Γ point all the matrices $T_{x,y,z}$ vanish identically. Thus, the higher s-like state,

$$E_s^\Gamma = \frac{\epsilon_{s,\mathrm{Bi}} + \epsilon_{s,\mathrm{I}}}{2} + \sqrt{\left(\frac{\epsilon_{s,\mathrm{Bi}} - \epsilon_{s,\mathrm{I}}}{2}\right)^2 + 36t_{ss}^2}\,, \tag{4}$$

is out of H_s (Eq. 2) and is close to the Fermi level. Similarly, the lower p-like states,

$$E_p^\Gamma = \frac{\epsilon_{p,\mathrm{Bi}} + \epsilon_{p,\mathrm{I}}}{2} - \sqrt{\left(\frac{\epsilon_{p,\mathrm{Bi}} - \epsilon_{p,\mathrm{I}}}{2}\right)^2 + \left(2t_{pp}^\sigma + 4t_{pp}^\pi\right)^2}\,, \tag{5}$$

are obtained from $H_{p_{x,y,z}}$ and are triply degenerate due to the cubic symmetry. The states away from these levels are not relevant to the band touching. At the L point, it is less straightforward to obtain the band energies. Nevertheless, we show in the Supplemental Material that the eigenvalues contain two doublet at $\epsilon_{p,\mathrm{I}}$ and $\epsilon_{p,\mathrm{Bi}}$, respectively, and four nondegenerate states at $E_{a\pm}^L$ and $E_{b\pm}^L$ as a result of s-p mixings. It will be clear in a moment that the states,

$$E_{b\pm}^L = \frac{\epsilon_{s,\mathrm{Bi}} + \epsilon_{p,\mathrm{I}}}{2} \pm \sqrt{\left(\frac{\epsilon_{s,\mathrm{Bi}} - \epsilon_{p,\mathrm{I}}}{2}\right)^2 + 12t_{sp}^2}\,, \tag{6}$$

close to the Fermi level are relevant to the formation of band touching at the Γ point.

At the outset, the band structure may represent a trivial insulator [Fig.1(c)] in which the higher s band is below the lower p band and the Fermi level lies between them. This situation, $E_s^\Gamma < E_p^\Gamma$, occurs if the hopping t_{sp} is weak and the on-site energies have $\epsilon_{s,\mathrm{Bi}} \ll \epsilon_{p,\mathrm{I}}$. As we lift $\epsilon_{s,\mathrm{Bi}}$ toward $\epsilon_{p,\mathrm{I}}$, the s band at Γ can be above the p band [Fig.1(d)] once the condition $E_s^\Gamma > E_p^\Gamma$ is satisfied. To make a hole band emerge in the presence of the triple degeneracy at E_p^Γ, we may increase $|t_{sp}|$ so that the energy E_{b-}^L is pushed down below E_p^Γ. Therefore, the band touching at the Fermi level in Fig.1(e) is realized if

$$E_s^\Gamma > E_p^\Gamma > E_{b-}^L\,. \tag{7}$$

The important parameters concerning above condition are the energy difference $\epsilon_{p,\mathrm{I}} - \epsilon_{s,\mathrm{Bi}}$ and the hopping amplitude $|t_{sp}|$. Finally, we restore the spin degree of freedom and turn on the SOC. Fig.1(f) displays the gap opening at Γ in the presence of SOC in the form $\lambda\vec{L}\cdot\vec{s}$.

Aided by the color code in Fig.1(c)-(f) representing the weight of s character of the corresponding Bloch state, one can notice a complete topological phase transition from (c) to (f). Focus on the Γ point. Since the Bloch state just below the Fermi level changes from the s character in (c) to the p character in (f), we may conclude that the Z_2 invariant [43] associated with Fig.1(c) and (f) must be different and hence the two states must represent

Compound	a=b=c($\AA$)	$\alpha = \gamma = \beta(^\circ)$	E_{gap} (eV)
Ba_2BiIO_6	6.241	60	0.55
Sr_2BiIO_6	6.169	60	0.53
Ca_2BiIO_6	6.123	60	0.52
Ba_2BiBrO_6	6.102	60	0.33
Sr_2BiBrO_6	6.009	60	0.32
Ca_2BiBrO_6	5.951	60	0.34

TABLE I. The optimized lattice parameters of the primitive cell of A_2BiXO_6 and their calculated band gaps E_{gap}.

distinct phases. In the followings, we shall specifically focus on the double perovskites and show that the above tight-binding model is essential to their band structure and topological property.

Band Structure and Z_2 Invariant. The class of materials A_2BiXO_6 in double perovskite structure is shown in the Fig.2(a) and its primitive Brillouin zone in Fig.2(b). The unit cell contains the octahedra BiO_6 and XO_6 at the corners of rock-salt lattice and the cation A is surrounded by these octahedra. Determined by the electron negativity of the constituent, the charge state in the ionic limit can be assigned as: A^{2+}, Bi^{3+}, X^{5+}, and O^{2-}. Using the first-principles package VASP [37] with generalized gradient approximation (GGA) for the correlation functional [38], projector augmented wave method (PAW) for core electrons [39], $10 \times 10 \times 10$ for k-sampling integration [40] and 500eV for energy cutoff, we find a total of six TIs out of a large number of possible double perovskites (Ca,Sr,Ba)$_2$BB'O_6 with B and B' from the III to VII families. The optimized lattice parameters and the band gaps with SOC are listed in Table I.

Fig.2(c) shows the band structures of the six TIs A_2BiXO_6. The band structures barely change as the A-site elements vary. However, the band gap is sensitive to the choice of X. Since the SOC is weaker in Br than in I, the band gap in the materials with Br is only 60% of those with I. A key feature of these band structures is the band touching at the Γ-point in the absence of SOC. Clearly, the triple degeneracy is resolved into a doublet and a singlet in the presence of SOC, which is consistent with the previous TB model.

To examine the topological feature of these materials, we implement the n-field method of

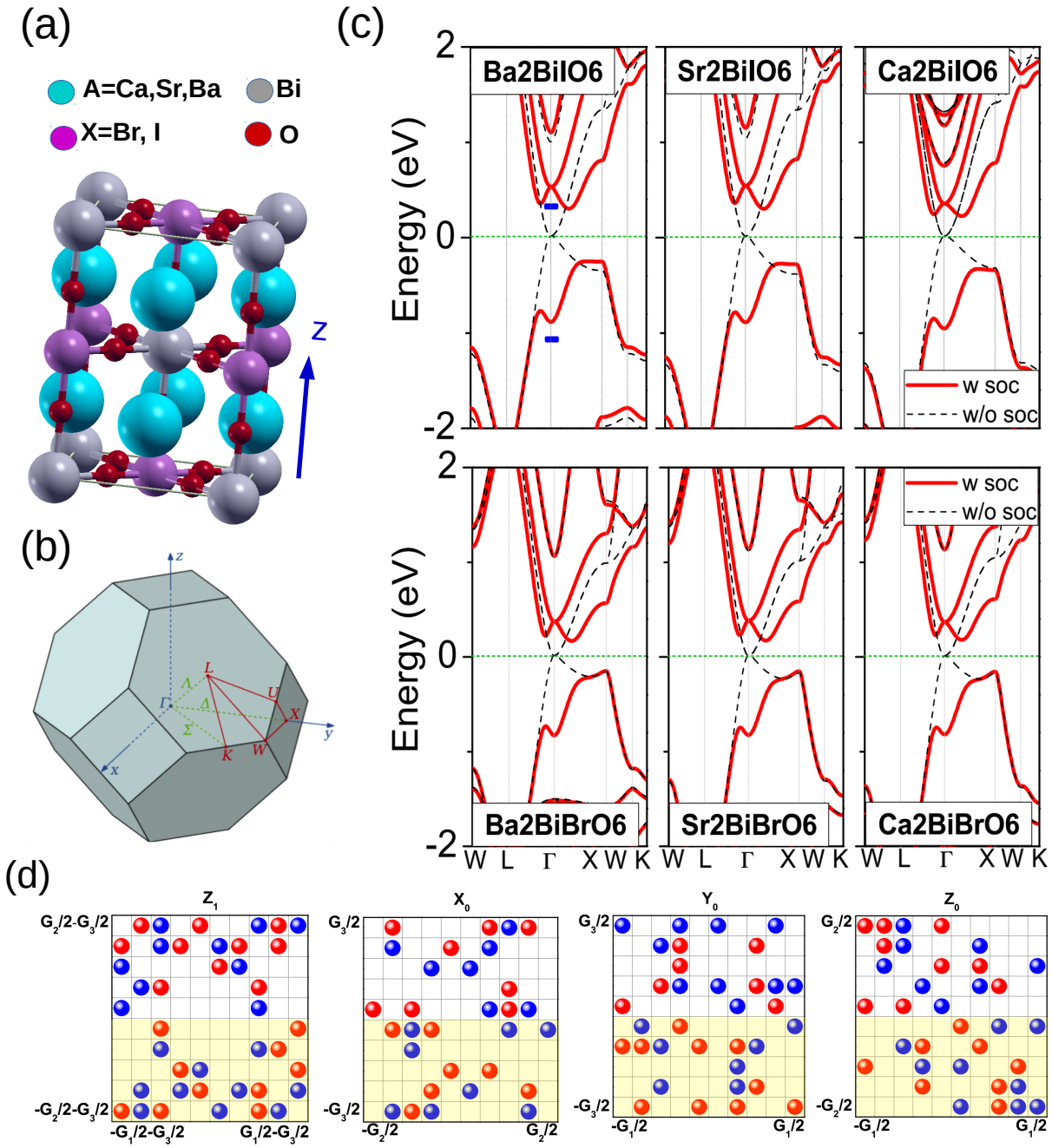

FIG. 2. (color online) (a) Crystal structure of double perovskite $ABiXO_6$ (b) Primitive Brillouin zone of double perovskite structure (c) Band structure of various A_2BiXO_6 materials (d) n-field diagrams of the representative material Ba_2BiIO_6. The n-field diagrams read $Z_1 = 0$, $Z_0 = 1$, $X_0 = 1$ and $Y_0 = 1$. Using the relation $X_0 + X_1 = Y_0 + Y_1 = Z_0 + Z_1$ and $(\nu_0; \nu_1\ \nu_2\ \nu_3) = (Z_0 + Z_1; X_1\ Y_1\ Z_1)$ mod 2, we get the Z_2 invariant $(\nu_0; \nu_1\ \nu_2\ \nu_3) = (1; 0\ 0\ 0)$.

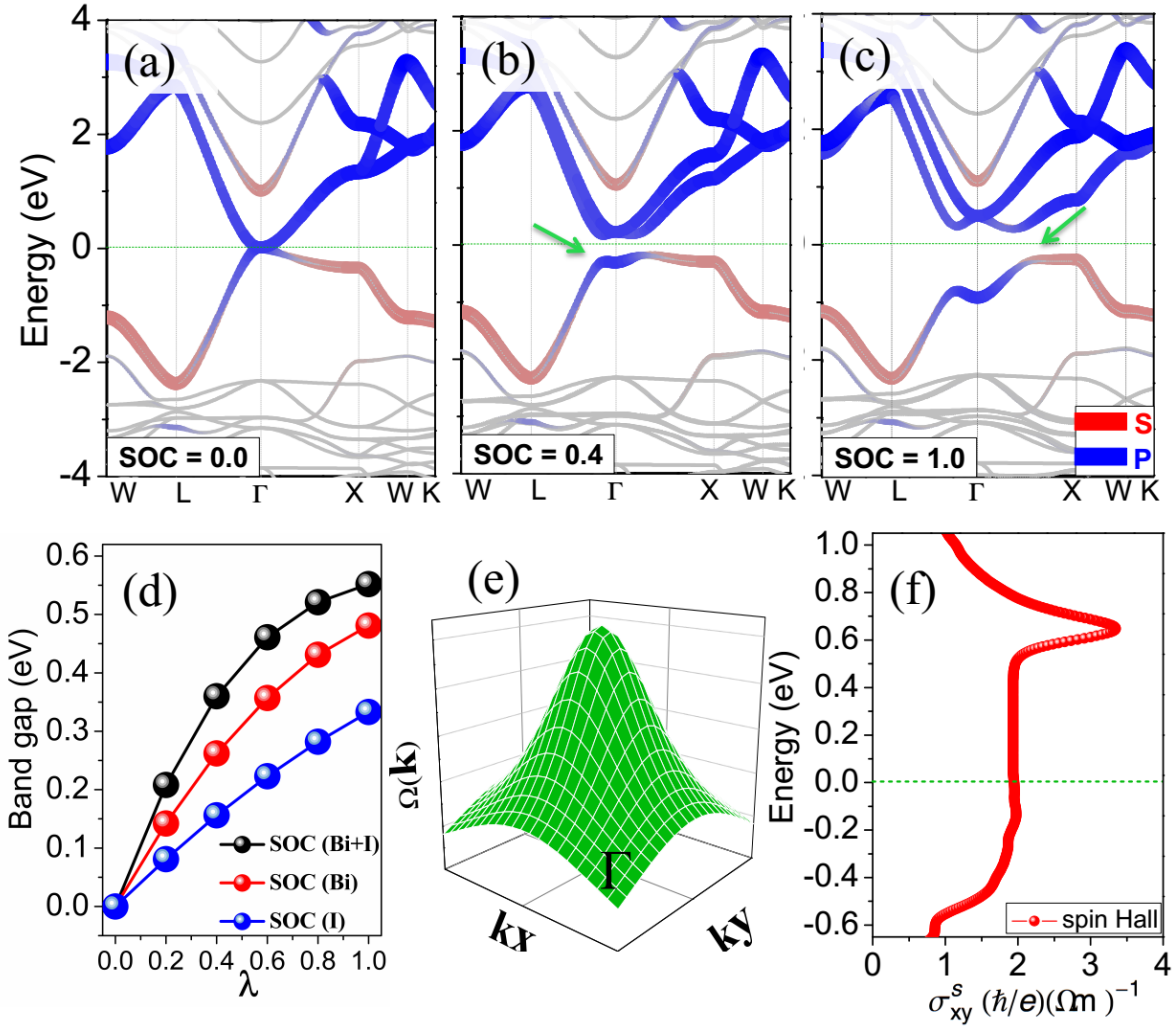

FIG. 3. (color online) Evolution of band structure of Ba_2BiIO_6 as SOC is gradually turned on [(a) to (c)]. Colored intensity shows the component of s-orbital and p-orbital on Bi and I. In (a), the band inversion at Γ clearly appears even if SOC is turned off. Arrows indicate the k-point where narrowest gaps appear. Inset shows the band gap while tuning the SOC. (d) shows the band gaps when tuning the strength of SOC of Bi and I respectively. (e) displays the calculated spin Berry curvature around Γ-point and (f) the spin Hall conductance as a function of Fermi energy.

evaluating the Z_2 invariant proposed by Fukui et. al. [41, 42]. The resultant n-field diagrams of a representative material Ba_2BiIO_6 are shown in Fig.2(d). We found that the six materials share the same Z_2 invariants $(\nu_0;\ \nu_1\ \nu_2\ \nu_3) = (1;\ 0\ 0\ 0)$, indicating that all the six materials are strong TIs. On the other hand, Fu and Kane proposed another method to obtain the Z_2 invariant for crystals with inversion symmetry by evaluating the parity eigenvalues of

Λ_i	Λ_{000}	Λ_{100}	Λ_{010}	Λ_{110}	Λ_{001}	Λ_{101}	Λ_{011}	Λ_{111}
ξ_v	−	−	−	+	−	+	+	−
ξ_c	−	+	+	−	+	−	−	+
$\delta(\Lambda_i)$	−	−	−	+	−	+	+	−

TABLE II. The topological invariant δ associated with the occupied bands at eight TRIM's Λ_i and the parity eigenvalues of the Bloch states just below (ξ_v) and above (ξ_c) the Fermi level.

the occupied bands [43]. Table II displays the invariant $\delta(\Lambda_i)$ associated with the full set of occupied bands of Ba_2BiIO_6 at the eight time-reversal invariant momenta (TRIM) Λ_i as well as the parity eigenvalues ξ_v (ξ_c) of the band just below (above) the Fermi level. We thus obtain the same topological invariant (ν_0; ν_1 ν_2 ν_3) = (1; 0 0 0), consistent with the n-field method.

Next, we continue with studying the band characters near the Fermi level. The respective weight of s- and p-components of the Bloch states are calculated by DFT and are shown by the color code in Fig. 3 in which the SOC is gradually turned on to its full strength. In the case of vanishing SOC [Fig. 3(a)], the lowest conduction band is composed of p-orbitals only while the highest valence band has the main component from s-orbitals except near the Γ point. From the aspect of Z_2 invariant, one may regard this state as a TI with zero band gap. According to Fig. 3(b) and (c), as the SOC is gradually turned on, the size of band gap increases accordingly while the band character remains, eventually leading to a giant band gap [Fig. 3(d)]. It is important to note that the SOC in this class of materials *does not* serve to exchange the band character, or the parity eigenvalue, unlike what it does in conventional TI Bi_2Se_3. To further clearly identify the non-trivial topology, we also calculate the spin Berry curvature [Fig. 3(e)] associated with the occupied band and the resultant spin Hall conductance [Fig. 3(f)] as a function of Fermi energy. The quantized values of spin Hall conductance within the SOC gap demonstrates the critical features of the topological phase.

Surface states. Another benchmark of a TI is the presence of linear dispersion within the bulk gap representing the Dirac electron on the surface. To investigate the surface states, we consider the semi-infinite slab structure with two types of surface. The one at top is terminated at the Ba-O layer while the one at bottom is at Bi-I-O layer, which is shown in Fig. 4(a). A tight-binding Hamiltonian is constructed with the maximally localized

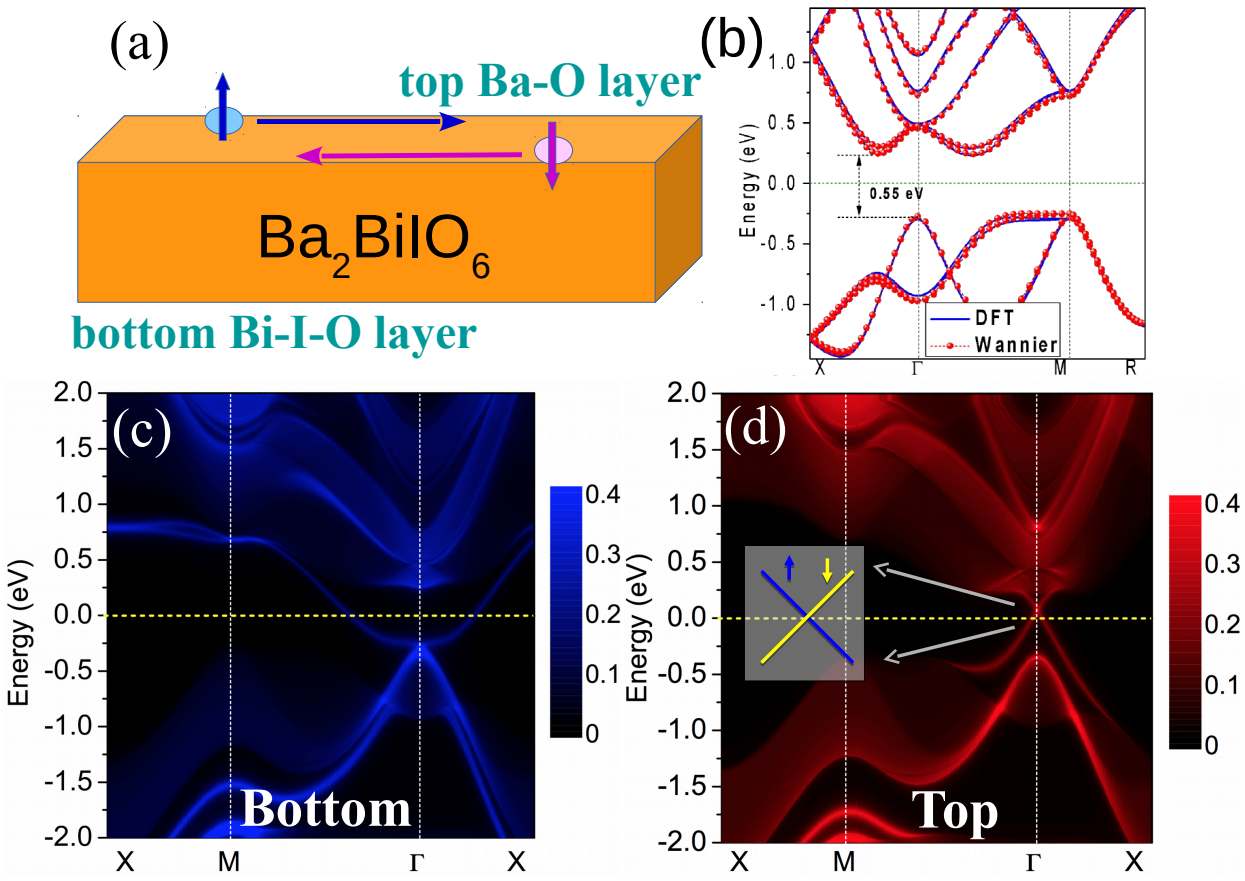

FIG. 4. (color online) Surface band structure of Ba_2BiIO_6 using Wannier functions. (a) slab geometry in our calculation. For Wannier calculation, thickness d=∞; for first-principles calculation, d=4nm. (b) displays the bulk band structure from Wannier functions. (c) spectrum of the top surface (Ba-O layer termination). (d) spectrum of the bottom surface (Bi-O-I layer termination).

Wannier functions (MLWFs) using WANNIER90 package [44]. The bulk band structures from MLWF are shown in Fig. 4(b), showing excellent agreement comparing to DFT bands. The surface spectral weight of the semi-infinite slab is computed by the surface Green's function method [45–47]. Surprisingly, as shown in Fig. 4(c), a non-Dirac-like dispersion appears at the bottom Bi-I-O layer at which dangling bonds present. Since the Bloch states around the Fermi level have significant components falling on Bi and I atoms, the presence of dangling bond may greatly alter the wavefunctions and the surface states. On the other hand, as shown in Fig. 4(d), a Dirac-like spectrum is clearly presented on the top surface terminated by Ba-O layer since the Bloch states associated with Ba are away from the Fermi energy. It is worthy mentioning that the Ba-O layer may be regarded as a cap layer that

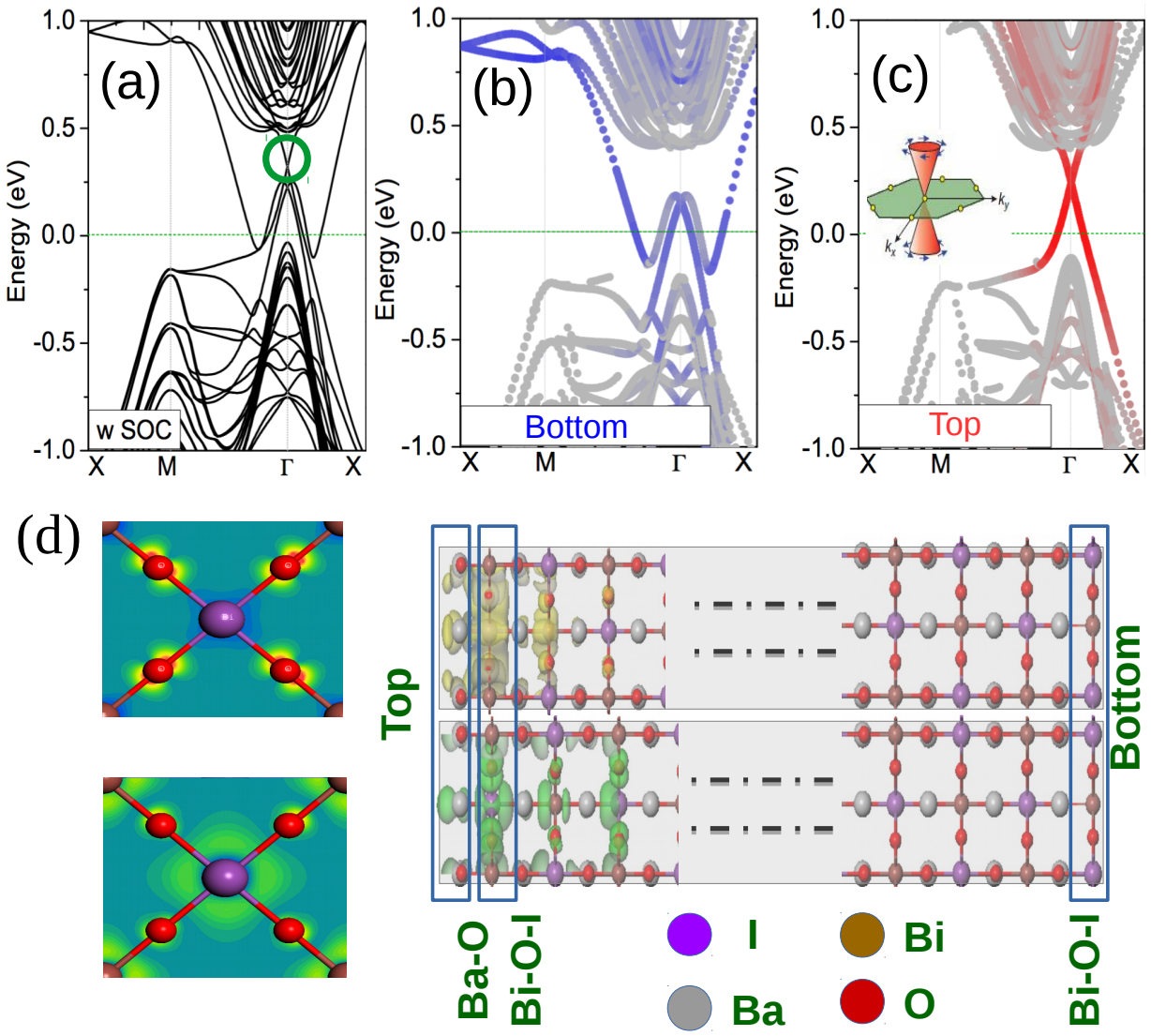

FIG. 5. (color online) Surface band structure of Ba_2BiIO_6 using DFT calculation. (a) the full band structure of the slab geometry (b) projected spectrum on the bottom surface (Bi-O-I layer). (c) projected spectrum on the top surface (top second Bi-O-I layer). Inset shows the helical state feature. (d) the spatial wave functions of the two states at the Dirac points circled in (a). Left panel: the top view of the Bi-I-O layer. Right panel: the side view of the slab geometry.

protects the Dirac state from the severe perturbation due to the dangling bond.

Although Wannier functions method is commonly used to explore the surface states, [23] it is usually considered as an artificial calculation because it uses the tight-binding parameters obtained from the bulk band structure without taking the interface effects such as surface energy renormalization and dangling bonds into account. To address this issue, we also

perform the DFT calculation of a slab geometry in which 5 unit cells of Fig.2(a) are repeated along the z-axis. It corresponds to the thickness about 4 nm, which has been proven large enough against the interactions between top and bottom surfaces based on our Wannier function projected bands of analysis. The band structure of the slab geometry is shown in Fig.5(a). In Fig.5(b) for the bottom surface, a distorted in-gap Dirac spectrum state emerges around the Γ-point. [48] Instead, the Dirac state on the top surface [Fig.5(c)] is more transparent and consistent with the Wannier-function analysis in previous paragraph. According to our TB model and DFT calculation, the bulk states around the Fermi level are mainly contributed by the *s*- and *p*-orbitals of Bi and I atoms. When the bottom Bi-O-I layer is exposed, the dangling bonds certainly alter the states around the Fermi level, which might result in the distortion of the Dirac state. As for the case with Ba-O layer at the termination, the associated dangling bonds can only perturb the states away from the Fermi level, leaving the surface Dirac states and the Kramers doublets intact. Hence we expect the class of materials with surfaces terminated at A-O layers to possess the topological features and superior surface transport property. In fact, the Ba-O layer termination is also more structurally stable because the breaking of BiO_6 or IO_6 octahedra requires more energy, making the top Ba-O surface more feasible during the synthesis process. We have also plotted the 3D spatial wave functions of the Dirac state [circled in Fig.5(a)] in Fig.5(d) showing a highly localized behavior on the top second Bi-O-I layer. The 2D projections of surface wave functions clearly exhibit the *s*- and *p*-characters also in agreement with our previous discussion.

Discussion. One distinct feature of our proposed 3D TIs is that it is intrinsic TIs with the Fermi level lying in the giant non-trivial SOC gap. To consider a more realistic situation, the robustness of TI states against surface reconstruction has also been studied. As shown in Fig. S1 in Supplementary Material, one can see that surface relaxation mainly induces charge redistribution between the bottom and top surface from the shifting of Fermi level, leaving the main features of Dirac states unchanged. Experimentally, one can detect the topological surface states by measuring the quantized conductance protected by the topological nature, or by mapping out the surface state of solids in the reciprocal space by the state-of-art Angle-resolved photoemission spectroscopy (ARPES). Since the energy position of these surface states can be easily tuned by applying electric field, one may switch between electron and hole transport on the surfaces as well. Moreover, doping to double perovskite structure can also be

implemented by replacing the A2+ cations with A1+ or A3+ ones of similar size [31], which makes the Bloch states near the Fermi level intact while little disorder is introduced to the system. Thus, the doped compounds can be converted into topological superconductor [49, 50] at sufficiently low temperature, which has immense impact on the fundamental physics of non-Abelian particles and fault-tolerant quantum computations [51]. We believe that our work may provide an interesting platform and stimulate new experimental investigations of double-pervoskite structures in many other new directions.

Summary. By proposing a generic tight-binding model for rock-salt lattice, we have shown a new notion of topological phase transition from a trivial state in Fig.1(c) to the topological state in (f) of 3D materials with strong SOC and cubic symmetry. With the band touching and band inversion in the band structure without SOC, it turns out that the SOC becomes more effective in generating a giant band gap of a TI. We further suggest possible realization of our model in well-known double perovskites A_2BiXO_6 (A=Ca, Sr, Ba; X=I, Br) by doping V and VII elements into B and B$'$ site, with non-trivial band gap as large as 0.55eV. Further analysis on the surface states shows that the surface Dirac cone is stable on surface terminated by A and oxygen atoms and robust against surface reconstruction, providing stable TIs states for experimental realization. Our findings not only enrich the physics of TIs realm but also open a new vista of searching for new TIs in new dimensions. Our proposed materials hold great potential to realize a new paragon of 3D TIs for practical applications.

ACKNOWLEDGEMENT

Useful conversation with M. Kennett is acknowledged. Work at National Taiwan Normal University was supported by Taiwan Ministry of Science and Technology through Grant No. 103-2112-M-003-012-MY3 and No. 103-2112-M-003-005. Work at University of California, Irvine was supported by DOE-BES (Grants No. DE-FG02-05ER46237 for H.W. and No. SC0012670 for S.P.). Computer simulations were partially supported by NERSC and National Center for High-Performance Computing of Taiwan.

AUTHOR CONTRIBUTIONS

YKW performed preliminary search of the materials. CKL developed the tight-binding model. HW, STP and JWK performed the analysis of the electronic structutre and topological properties. CKL, STP and HW discussed the results and wrote the maniscript. RQW, CKL and YKW supervised the project.

---

* Contributed equally to this work

† wur@uci.edu

‡ kant@ntnu.edu.tw

§ Lu49@ntnu.edu.tw

[1] von Klitzing, K., Dorda, G. & Pepper, M. New method for high-accuracy determination of the fine-structure constant based on quantized Hall resistance. *Phys. Rev. Lett.* **45**, 494 (1980).

[2] Haldane, F. D. M. Model for a quantum Hall effect without Landau levels: condensed-matter realization of the "parity anomaly". *Phys. Rev. Lett.* **61**, 2015 (1988).

[3] Kane, C. L. & Mele, E. J. Quantum spin Hall effect in graphene. *Phys. Rev. Lett.* **95**, 226801 (2005).

[4] Bernevig, B. A. & Zhang, S.-C., Quantum spin Hall effect. *Phys. Rev. Lett.* **96**, 106802 (2006).

[5] Pi. S.-T. & Savrasov, S. Y. Polarization induced Z_2 and Chern topological phases in a periodically driving field. *Sci. Rep.* **6**, 22993 (2016).

[6] Fu, L. Topological crystalline insulators. *Phys. Rev. Lett.* **2011**, 106, 106802.

[7] Wang, Z., Sun, Y., Chen, X.-Q., Franchini, C., Xu, G., Weng, H., Dai, X. & Fang, Z. Dirac semimetal and topological phase transitions in A_3Bi (A=Na, K, Rb). *Phys. Rev. B* **85**, 195320 (2012).

[8] Wang, Z., Weng, H., Wu, Q., Dai, X. & Fang, Z. Three-dimensional Dirac semimetal and quantum transport in Cd_3As_2. *Phys. Rev. B* **88**, 125427 (2013).

[9] Wan, X., Turner, A. M., Vishwanath, A. & Savrasov, S. Y. Topological semimetal and Fermi-arc surface states in the electronic structure of pyrochlore iridates. *Phys. Rev. B* **83**, 205101 (2011).

[10] Xu, S.-Y., Belopolski, I., Alidoust, N., Neupane, M., Bian, G., Zhang, C., Sankar, R., Chang, G., Yuan, Z., Lee, C.-C., Huang, S.-M., Zheng, H., Ma. J., Sanchez, D. S., Wang, B., Bansil, A., Chou, F., Shibayev, P. P., Lin, H., Jia, S. & Hasan, M. Z. Discovery of a Weyl fermion semimetal and topological Fermi arcs. *Science* **349**, 613-617 (2015).

[11] Thouless, D. J., Kohmoto, M., Nightingale, M. P. & den Nijs, M. Quantized Hall conductance in a two-dimensional periodic potential. *Phys. Rev. Lett.* **49**, 405 (1982).

[12] Schnyder, A. P., Ryu, S., Furusaki, A. & Ludwig, A. W. W. Classification of topological insulators and superconductors in three spatial dimensions. *Phys. Rev. B* **78**, 195125 (2008).

[13] Yang B.-J. & Nagaosa, N. Classification of stable three-dimensional Dirac semimetals with nontrivial topology. *Nat. Communication* **5**, 4898 (2014).

[14] Fu L. & Kane, C. L. Superconducting proximity effect and Majorana fermions at the surface of a topological insulator. *Phys. Rev. Lett.* **100**, 096407 (2008).

[15] Qi, X.-L., Li, R., Zang, J, & Zhang, S.-C. Inducing a magnetic monopole with topological surface states. *Science* **323**, 1184-1187 (2009).

[16] Checkelsky, J. G., Ye, J., Onose, Y., Iwasa, Y. & Tokura, Y. Dirac-fermion-mediated ferromagnetism in a topological insulator. *Nat. Phys.* **8**, 729-733 (2012).

[17] Zhang, J., Chang, C.-Z., Tang, P., Zhang, Z., Feng, X., Li, K., Wang, L.-L., Chen, X., Liu, C., Duan, W., He, K., Xue, Q.-K., Ma, X. & Wang, Y. Topology-driven magnetic quantum phase transition in topological insulators. *Science* **339**, 1582-1586 (2013).

[18] Hasan, M. Z. & Kane, C. L. *Colloquium*: Topological insulators. *Rev. Mod. Phys.* **82**, 3045 (2010).

[19] Ando, Y. Topological insulator materials. *J. Phys. Soc. Jpn.* **82**, 102001 (2013).

[20] Hor, Y. S., Richardella, A., Roushan, P., Xia, Y., Checkelsky, J. G., Yazdani, A., Hasan, M. Z., Ong, N. P. & Cava, R. J. *p*-type Bi_2Se_3 for topological insulator and low-temperature thermoelectric applications. *Phys. Rev. B* **79**, 195208 (2009).

[21] Xu, Y., Gan, Z. & Zhang, S.-C., Enhanced thermoelectric performance and anomalous Seebeck effects in topological insulators. *Phys. Rev. Lett.* **112**, 226801 (2014).

[22] Pal, K., Anand, S. & Waghmare, U. V. Thermoelectric properties of materials with nontrivial electronic topology. *J. Mater. Chem. C* **3**, 12130-12139 (2015).

[23] Zhang, H., Liu, C.-X., Qi, X.-L., Dai, X., Fang, Z. & Zhang, S.-C. Topological insulator in Bi_2Se_3, Bi_2Te_3, and Sb_2Te_3 with a single Dirac cone on the surface. *Nat. Phys.* **5**, 438-442

(2009).

[24] Hu, J., Alicea, J., Wu, R Q. & Franz, M. Giant topological insulator gap in graphene with $5d$ adatoms. *Phys. Rev. Lett.* **109**, 266801 (2012).

[25] Ma, Y., Dai, Y. & Niu, C., Huang, B. Halogenated two-dimensional germanium: candidate materials for being of quantum spin Hall state. *J. Mater. Chem.* **22**, 12587-12591 (2012).

[26] Wang, H., Pi, S.-T., Kim, J., Wang, Z., Fu, H. H. & Wu, R. Q. Possibility of realizing quantum spin Hall effect at room temperature in stanene/Al_2O_3(0001). *Phys. Rev. B* **94**, 035112 (2016).

[27] Murakami, S. Phase transition between the quantum spin Hall and insulator phases in 3D: emergence of a topological gapless phase. *New J. Phys.* **9**, 356 (2007).

[28] Vafek O. & Yang, K. Many-body instability of Coulomb interacting bilayer graphene: Renormalization group approach. *Phys. Rev. B* **81**, 041401(R) (2009).

[29] Sun, S., Yao, H., Fradkin, E. & Kivelson, S. A. Topological insulators and nematic phases from spontaneous symmetry breaking in 2D Fermi systems with a quadratic band crossing. *Phys. Rev. Lett.* **103**, 046811 (2009).

[30] Yamaji Y. & Imada, M. Metallic interface emerging at magnetic domain wall of antiferromagnetic insulator: Fate of extinct Weyl electrons. *Phys. Rev. X* **4**, 021035 (2014).

[31] Vasala S. & Karppinen, M. $A_2B'B''O_6$ perovskites: A review. *Prog. in Solid State Chem.* **43**, 1-36 (2015).

[32] Kim, B. J., Jin, H., Moon, S. J., Kim, J.-Y., Park, B.-G., Leem, C. S., Yu, J., Noh, T. W., Kim, C., Oh, S.-J., Park, J.-H., Durairaj, V., Cao, G. & Rotenberg, E. Novel $J_{\rm eff} = 1/2$ Mott state induced by relativistic spin-orbit coupling in Sr_2IrO_4. *Phys. Rev. Lett.* **101**, 076402 (2008).

[33] Kojima, A., Teshima, K., Shirai, Y. & Miyasaka, T. Organometal halide perovskites as visible-light sensitizers for photovoltaic cells. *J. Am. Chem. Soc.* **131**, 6050-6051 (2009).

[34] Burschka, J., Pellet, N., Moon, S.-J., Humphry-Baker, R., Gao, P., Nazeeruddin, M. K. & Gratzel, M. Sequential deposition as a route to high-performance perovskite-sensitized solar cells. *Nature* **499**, 316-319 (2013).

[35] Jin, H., Im, J. & Freeman, A. J. Topological insulator phase in halide perovskite structures. *Phys. Rev. B* **86**, 121102(R) (2012).

[36] Yan, B., Jasen, M. & Felser, C. A large-energy-gap oxide topological insulator based on the superconductor $BaBiO_3$. *Nat. Phys.* **9**, 709-711 (2013).

[37] Kresse, G. & Hafner, J. *Ab initio* molecular-dynamics simulation of the liquid-metal-amorphous-semiconductor transition in germanium. *Phys. Rev. B* **49**, 14251 (1994).

[38] Perdew, J. P., Burke, K. & Ernzerhof, M. Generalized gradient approximation made simple. *Phys. Rev. Lett.* **77**, 3865 (1996).

[39] Kresse, G. & Joubert, D. From ultrasoft pseudopotentials to the projector augmented-wave method. *Phys. Rev. B* **59**, 1758 (1999).; Blochl, P. E. Projector augmented-wave method. *Phys. Rev. B* **50**, 17953 (1994).

[40] Monkhorst, H. J. & Pack, J. D. Special points for Brillouin-zone integrations. *Phys. Rev. B* **13**, 5188 (1976).

[41] Fukui, T., Hatsugai, Y. & Suzuki, H. Chern numbers in discretized Brillouin zone: Efficient method of computing (spin) Hall conductances. *J. Phys. Soc. Jap.* **74**, 1674-1677 (2005).

[42] Fukui T. & Hatsugai, Y. Quantum spin Hall effect in three dimensional materials: Lattice computation of Z_2 topological invariants and its application to Bi and Sb. *J. Phys. Soc. Jap.* **76**, 053702 (2007).

[43] Fu, L. & Kane, C. L. Topological insulators with inversion symmetry. *Phys. Rev. B* **76**, 045302 (2007).

[44] Mostofi, A. A., Yates, J. R., Pizzi, G., Lee, Y. S., Souza, I., Vanderbilt, D. & Marzari, N. An updated version of wannier90: A tool for obtaining maximally-localised Wannier functions. *Comput. Phys. Commun.* **185**, 2309-2310 (2014).

[45] Sancho, M. P. L., Sancho, J. M. L. & Rubio, J. Quick iterative scheme for the calculation of transfer matrices: application to Mo (100). *J. of Phys. F: Metal Physics* **14**, 1205-1215 (1984).

[46] Sancho, M. P. L., Sancho, J. M. L., Sancho, J. M. L. & Rubio, J. Highly convergent schemes for the calculation of bulk and surface Green functions. *J. of Phys. F: Metal Physics* **15**, 851 (1985).

[47] Lee P., Kim, J., Kim, J., Ryu, M., Park, H., Kim, N., Kim, Y., Lee, N., Kioussis, N., Jhi, S. & Chung, J. Topological modification of the electronic structure by Bi-bilayers lying deep inside bulk Bi_2Se_3. *J. Phys.: Condens. Matter* **28**, 085002 (2016).

[48] This distorted Dirac surface states actually resemble those appear on the surface of Bi_2Te_3, see Fig. 8(b) in Ref. [19]

[49] Hor, Y. S., Williams, A .J., Checkelsky, J. G., Roushan, P., Seo, J., Xu, Q., Zandbergen, H. W., Yazdani, A., Ong, N. P. & Cava, R. J., Superconductivity in $Cu_xBi_2Se_3$ and its implications

for pairing in the undoped topological insulator. *Phys. Rev. Lett.* **104**, 057001 (2010).

[50] Fu, L. & Berg, E. Odd-parity topological superconductors: Theory and application to $Cu_xBi_2Se_3$. *Phys. Rev. Lett.* **105**, 0097001 (2010).

[51] Ivanov, D. A. Non-Abelian statistics of half-quantum vortices in p-wave superconductors. *Phys. Rev. Lett.* **86**, 268 (2001).